

## Electronic Supplementary Information (ESI)

### **Three-Dimensional Plasmonic Spacer Enables Highly Efficient Solar-Enhanced Membrane Distillation of Seawater**

Edison Huixiang Ang<sup>\*\*†</sup>, Yong Zen Tan<sup>†</sup>, and Jia Wei Chew<sup>\*a</sup>

<sup>a</sup>School of Chemical and Biomedical Engineering, Nanyang Technological University, Singapore 637459, Singapore.

<sup>†</sup> These authors contribute equally to this work.

\*Corresponding author at e-mail: [jchew@ntu.edu.sg](mailto:jchew@ntu.edu.sg); Tel: +65 63168916

\*\*Co-corresponding author at e-mail: [angh0040@e.ntu.edu.sg](mailto:angh0040@e.ntu.edu.sg); Tel: +65 6908 1436

## Experimental Section

**Fabrication process for the 3D plasmonic spacers:** The binder-free plasmonic spacers were prepared by a two-step approach. The Pt NSs were first grown directly on NF based on our previously reported thermal decomposition method<sup>[18]</sup> and then washed in water by sonication, resulting in the Pt NSs/NF spacer. Subsequently, the Ag NPs were deposited on the Pt NSs/NF spacer based on the chemical reduction method using borohydride to form the Pt@Ag NSs/NF, while adding 4,8-Bis(methylthio)benzo[1,2-d:4,5-d']bis[1,3]dithiole-2,6-dithione (MBT, Sigma Aldrich) during this step to fabricate the Pt-MBT@Ag NSs/NF. A piece of nickel foam (ACME Research Support Pte Ltd.) with dimensions (5.3 cm × 7 cm × 0.16 cm) was first cleaned with acetone and deionized water. Thermal decomposition was then carried out in a solvent mixture of ethanol and 2-propanol (1:1 v/v) containing 5 mM of chloroplatinic acid hexahydrate (Alfa Aesar) at 450 °C for 15 min purging with 95% Ar:5% H<sub>2</sub> gas. Subsequently, the as-prepared Pt NSs/NF were submerged in a solution (1:9 v/v of ethanol and deionized water) containing MBT and silver nitrate (Sigma Aldrich) precursors with the same molarity as the platinum precursor, followed by drop-wise addition of 1 mM of sodium borohydride (Sigma Aldrich) into the solution. All solvents were of reagent grade and purchased from Sigma-Aldrich. Finally, the plasmonic spacers were washed repeatedly with deionized water before performing the solar-enhanced MD tests.

**Characterizations of 3D plasmonic spacers:** The morphology and structure of the 3D plasmonic materials were analysed using the FESEM (JEOL-6700F SEM) and TEM with STEM (JEOL, Model JEM-2100F). The chemical distribution was characterized using energy-dispersive EDX analyzer (Oxford Instruments, model 7426) and the thickness of the NS was measured using AFM (Bruker Multimode 8, operating using tapping mode) techniques. The crystal structure of the samples were analysed using XRD (D2 PHASER with LYNXEYE detector and Cu-K $\alpha$  irradiation of  $\lambda = 1.5406 \text{ \AA}$ ). The XPS measurements were performed using a monochromated X-ray source (AXIS-Hsi, Kratos Analytical X-ray photoelectron spectrometer with excitation source of Al K $\alpha = 1486.71 \text{ eV}$ ). The Ag/MBT/Pt composite was verified using inductively coupled plasma optical emission spectroscopy (ICPOES, Optima 8300 ICP-OES spectrometer, PerkinElmer) and carbon-hydrogen-nitrogen-sulphur (CHNS, Vario Micro Cube) elemental analyser. The absorption spectra of the plasmonic spacers were measured with Shimadzu UV3600 Plus spectrophotometer.

**Evaluation of solar-enhanced MD performances:** The solar desalination experiments were performed using a customized transparent cross-flow set-up (Section S2, Supporting Information). The total active membrane area was 37.1 cm<sup>2</sup>. The hydrophobic PVDF membrane (125  $\mu\text{m}$ -thick; 0.22  $\mu\text{m}$  pore diameter; 75% porosity) was purchased from Durapore<sup>®</sup>. MD experiments were carried out using pure water, saline water mixtures (namely, 0.5 M NaCl) and real seawater (Section S4, Supporting Information). The quantities of salts and TOC from the treated water were examined by conductivity meter (Eutech Instruments Cond500) and TOC analyser (Shimadzu TOC-L), respectively. The temperature of the inlet feed solution was 35 °C while the permeate was 20 °C. The feed and permeate flowrates was 250 ml min<sup>-1</sup>, unless otherwise stated. Three repeated experiments per spacer were carried out to obtain the error bars associated with the MD performance. The distillate flux was calculated as  $V/(A \times t)$ , where  $A$  is the effective area of the membrane,  $t$  is the MD duration, and  $V$  is the distillate volume.

### **S1. Characterization of the plasmonic spacer**

The formation of plasmonic spacers were carefully examined by X-ray diffraction (XRD), transmission electron microscope (TEM), electron-dispersive X-ray (EDX), selected area electron diffraction (SAED), atomic force microscope (AFM), and X-ray photoelectron spectroscopy (XPS). The XRD pattern confirmed the formation of Pt on NF and Pt/Ag-based composite on NF, as shown in Fig. S1a. The three distinct peaks at 45.5°, 52.8° and 77.3° are the characteristic peaks of Ni in the NF. The other three peaks at around 40.3°, 46.9° and 68.1° represent Pt/Ag, with the leftward shifts of the peaks with respect to Pt indicating the formation of the Pt/Ag heterostructure. We also observed roots-like structures protruding from the NSs (shown in Fig. S1b), with the EDX line scan (Fig. S1c) indicating that they were made of Ni. This implies that the NSs were strongly adhered on the Ni foam surface through these roots. Fig. S1d shows that the SAED pattern of the single NS is attributed to the (111) plane of both Pt and Ag, further confirming the formation of the Pt/Ag hybrid. The size distribution histogram (Fig. S1e) of Ag NPs on the Pt NSs was obtained by analyzing several TEM images, with the average Ag NP diameter found to be  $2.5 \pm 0.3$  nm in diameter. The AFM analysis (Fig. S1f) reveals the single NS had a thickness of 34 nm, indicating that the as-obtained sheet was in the nanoscale range. The lack of any change in the areas under the Pt (0) (71.5 and 74.4 eV) and Pt-S (72.4 and 75.8 eV) signals, as well as the increase of the S-Metal (161.8 and 163.1 eV) signal with respect to S-terminus (163 and 164.6 eV) after Ag NPs formation, implies that there was no direct contact between Pt and Ag metals (Fig. S1g-h). It is worth noting that the intensity of the S-terminus bond is lower than S-metal bond, which indicates that most of the MBT ligands are embedded in between the Ag/Pt hybrid rather than dangling on the surface of the metals.

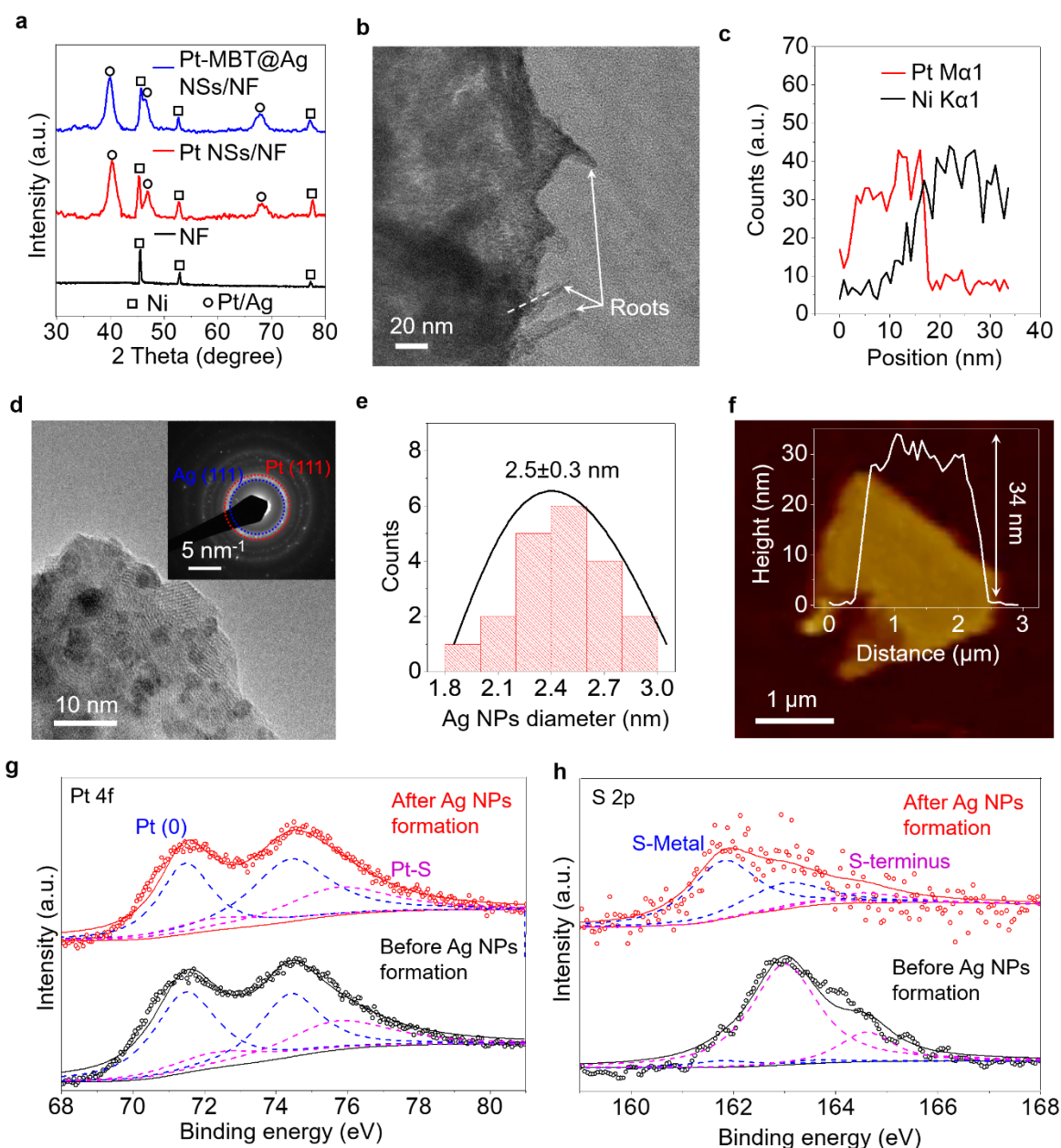


**Fig. S1** a) XRD pattern of NF, Pt NSs/NF, and Pt-MBT@Ag NSs/NF. b) TEM image of Pt NSs with Ni roots spotted at the edge. c) EDX line scan of the root at the edge of the NS labelled in white dash line in (b). d) High-resolution (HR)-TEM image of Pt-MBT@Ag NSs with inset SAED pattern of Ag (111) and Pt (111) planes labelled in blue and red dotted lines, respectively. e) an average NPs size distribution histogram, obtained by analysing multiple TEM images. f) AFM image of Pt-MBT@Ag NSs with its corresponding height profile (inset). g) Pt 4f and h) S 2p XPS spectra of MBT-grafted Pt NSs before and after Ag NPs formation.

Based on the Mie-theory calculations<sup>1</sup> and the thickness of the thin film<sup>2</sup> for Pt-MBT@Ag NSs grown on NF substrate, the theoretical and experimental visible spectra of their extinction, absorption, and scattering cross-sections were derived, as shown in Fig. S2. The air mass (AM) 1.5 solar irradiance is also shown as a reference. Clearly, in the Pt-MBT@Ag NSs structures, the absorption cross-section was larger than that of scattering, which is similar to previously reported plasmonic noble metal alloy.<sup>3</sup> In particular, the absorption spectrum of Pt-MBT@Ag peaks at 450 nm, which makes it an excellent absorber in the visible region of the electromagnetic spectrum and underlies its high photothermal efficiency.

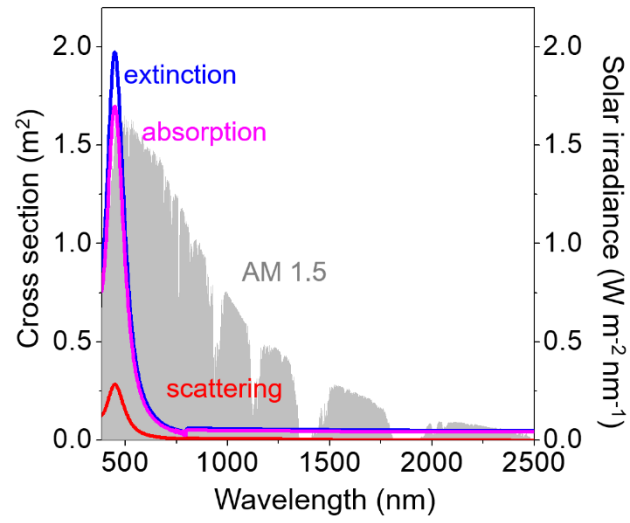


**Fig. S2** Theoretical and measured cross-sectional spectra of the Pt-MBT@Ag plasmonic spacers. Blue, pink, and red curves represent Mie-theory calculation of the extinction, absorption, and scattering cross-section, respectively. Grey area shows AM 1.5 solar irradiance as a reference.

## S2. Solar MD setup

The cross-flow direct contact MD module (Fig. S3a-b) was used to examine the separation performances and photothermal efficiencies of the plasmonic spacers. A Newport (model 91192, 1000 W) solar simulator with AM 1.5 global filter was used for the solar-enhanced MD experiments and a solar power meter (Tenmars TM-207) was used to measure the solar irradiance of the light. A power meter (UT230B-UK) was installed on the heater (Heidolph MR Hei-Tec) to deduce the energy consumed by the heater during light illumination and without light illumination. The pumps (Masterflex L/S Digital Drive) were integrated in the MD system to provide constant inflow and outflow of the feed and permeate solutions. The temperatures were monitored using K-type thermocouples (Cole-Palmer, US; labelled as "T" in Fig. S3b), while the chiller integrated with the heat exchanger (Julabo ME) was used to cool down and condense the water vapour. The amount of distillate collected per unit time was measured using a mass balance (Mettler-Toledo ME4002) and recorded using the LabVIEW software on a computer. Based on our preliminary results (Fig. S3c) on the effect of feed flowrate, distillate flux increased by 8% and photothermal efficiency decreased slightly by 1% when the feed flowrate increased from 100 ml min<sup>-1</sup> to 250 ml min<sup>-1</sup>, while distillate flux increased lesser by 4% and photothermal efficiency decreased drastically by ~20% when the feed flowrate increased from 250 ml min<sup>-1</sup> to 500 ml min<sup>-1</sup>. Therefore, the intermediate feed flowrate of 250 ml min<sup>-1</sup> was used based on the trade-off between distillate flux and photothermal efficiency, both of which are key parameters in the solar MD process.

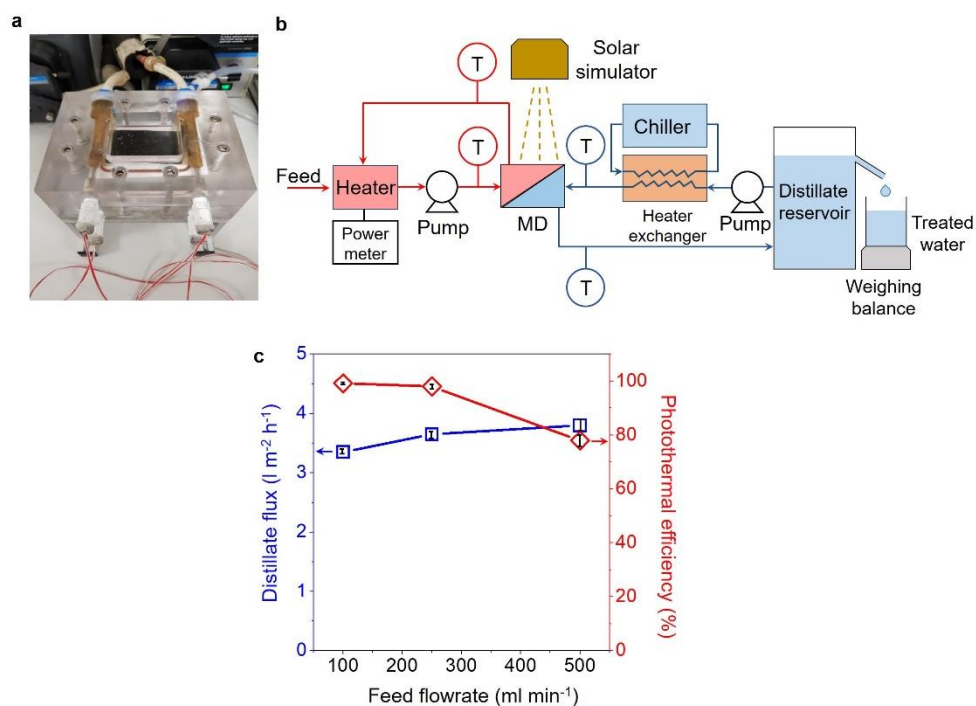


**Fig. S3** a) Solar-enhanced MD cell prototype. b) Schematic diagram of lab-scale MD setup. c) Distillate flux and photothermal efficiency versus feed flowrate of Pt-MBT@Ag NSs/NF spacer in MD.

### S3. Photothermal effect measurements of plasmonic spacer

As compared to the pristine NF, the as-prepared plasmonic spacers generally showed higher interface feed temperature (Fig. 2c) upon light illumination. This trend was consistent with the bulk temperature measurements when plasmonics were immersed in a 4 mm depth of flowing water (see Fig. S4a and Movie S1, Supporting Information) and under ambient air condition (Fig. S4b). Fig. S4a shows that the temperature of the Pt-MBT@Ag NSs/NF spacers immersed in water at a flowrate of  $250 \text{ ml min}^{-1}$  was slightly above the initial feed temperature of  $35 \text{ }^\circ\text{C}$ , indicating the occurrence of photothermal effects, whereas that of the pristine NF was below  $35 \text{ }^\circ\text{C}$  due to temperature polarization effects. Furthermore, we also evaluated the photothermal effect under ambient air (Fig. S4b), which indicates a more distinct temperature difference between the plasmonic spacer and the pristine NF, because of both the reflection of light by water and the continuous movement of the water that entered at  $35 \text{ }^\circ\text{C}$ .

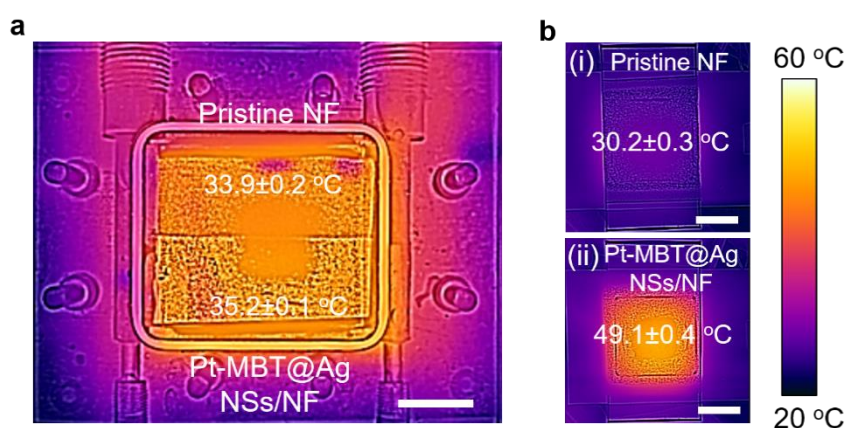


**Fig. S4.** a) Thermal image of pristine NF (top) and Pt-MBT@Ag NSs/NF (bottom) immersed in pure water with an initial feed temperature of  $35 \text{ }^\circ\text{C}$  at a constant flow of  $250 \text{ ml min}^{-1}$  under  $0.8 \text{ sun}$  illumination. Scale bar represents 2 cm. b) Thermal images of (i) pristine NF and (ii) Pt-MBT@Ag NSs/NF spacers under ambient air at  $0.8 \text{ sun}$  illumination. Light was shone from the bottom and thermal images were taken from the top. Scale bar represents 2 cm.

#### S4. Demo application: Seawater desalination

To test the feasibility of realistic implementation, we used real seawater collected at an island (Pulau Ubin) northeast of Singapore (Fig. S5) as the feed for the solar-enhanced MD with the Pt-MBT@Ag NSs/NF spacer. The inlet feed and permeate temperatures were respectively 35 °C and 20 °C, and the simulated solar flux used mimicked the variations throughout the day (note that solar flux data was collected outdoors from 0:00 to 24:00 on 9<sup>th</sup> May 2018). The chemical composition of the seawater was obtained using the ASTM standard test method (Table S1) and the treated water obtained was compared with some of the standards for drinkable water (see Table S2). Results show that the salt content (indicated by conductivity) reduced significantly from 49000 to 8  $\mu\text{S cm}^{-1}$  and TOC from 26 to 1.2  $\text{mg ml}^{-1}$ . Our treated water exhibited an extremely low ionic conductivity as well as TOC content, which are well below the standards for drinkable water, implying the superiority of the treatment method.

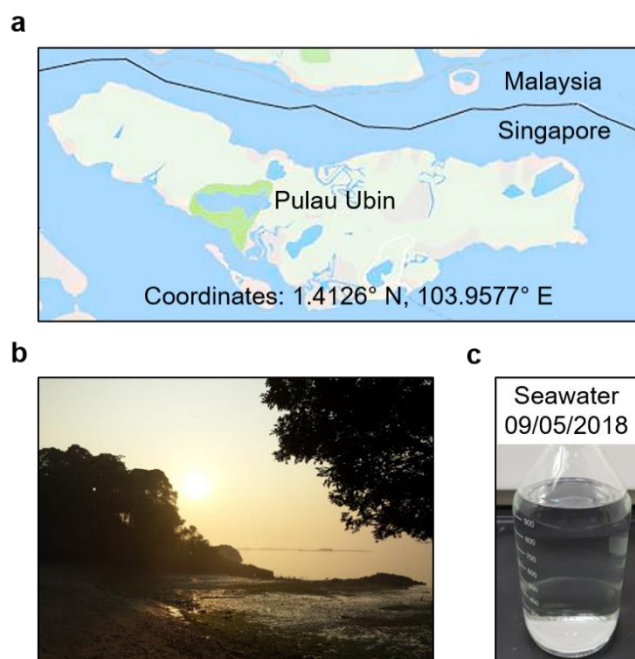


**Fig. S5** a) The seawater was collected from Pulau Ubin, a small island of Singapore (Copyright @Google Maps) at coordinates: 1.4126° N, 103.9577° E. b) Photograph of Pulau Ubin island in Singapore taken on May 9<sup>th</sup>, 2018 and c) picture of seawater contained in a glass bottle.

**Table S1.** Chemical composition of feed seawater (sea at Pulau Ubin island, Singapore)

Chemical	Content <sup>a)</sup>
Ca <sup>2+</sup> (ppm)	346
Mg <sup>2+</sup> (ppm)	1212
Na <sup>+</sup> (ppm)	7522
K <sup>+</sup> (ppm)	265
Cl <sup>-</sup> (ppm)	13333
Br <sup>-</sup> (ppm)	74
HCO <sub>3</sub> <sup>-</sup> (ppm)	146
SO <sub>4</sub> <sup>2-</sup> (ppm)	2155
Conductivity (μS cm <sup>-1</sup> )	49000
TOC (mg l <sup>-1</sup> )	26

<sup>a)</sup>Values obtained from ASTM standard test method.

**Table S2.** Standards for drinkable water

Standard	Conductivity (μS cm <sup>-1</sup> )	TOC <sup>d)</sup> (mg l <sup>-1</sup> )
WHO <sup>a)</sup>	1429	<2
EPA <sup>b)</sup>	571	<2
PUB <sup>c)</sup>	256	<2
This work	8	1.2

<sup>a)</sup>WHO: World Health Organization; <sup>b)</sup>EPA: Environmental Protection Agency; <sup>c)</sup>PUB: Public Utilities Board. <sup>d)</sup>TOC is total organic carbon.

### S5. Long-term durability tests of the plasmonic spacer for solar-enhanced MD

To test the durability of the plasmonic spacer (namely, Pt-MBT@Ag NSs/NF) for solar-enhanced MD, we ran the experiment with real seawater feed for a week using light illumination that mimics the outdoor solar irradiation throughout the day (Fig. 2f). At the end of seven days, the solar-enhanced MD exhibited similar rejection of salt (ion conductivity=  $\sim 0\text{--}1.3 \mu\text{S cm}^{-1}$ ) and TOC content ( $1.2\text{--}1.5 \text{ mg l}^{-1}$ ). It should be noted that these values are within the standards for drinkable water (shown in Table S2). Moreover, throughout the seven days, a constant distillate flux of  $\sim 60 \text{ l m}^{-2} \text{ day}^{-1}$  was obtained, giving a total volume of treated high-quality water of  $\sim 1.56 \text{ L}$ .

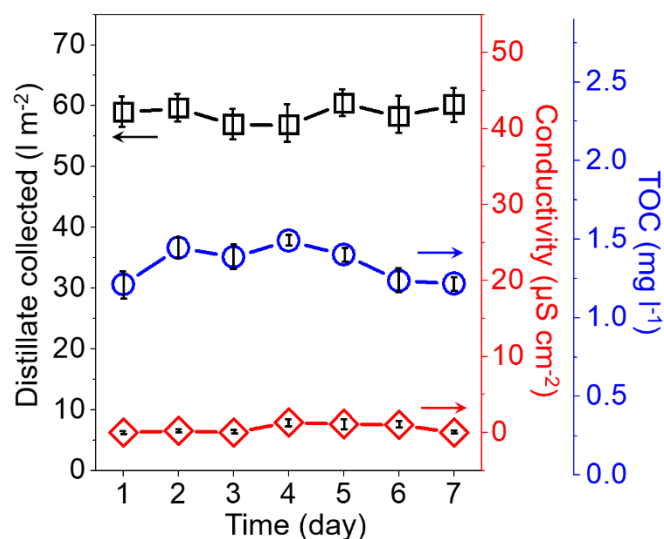


**Fig. S6** The solar MD containing Pt-MBT@Ag NSs/NF spacer was performed under the same conditions per day as presented in Fig. 2f and here it was conducted for a longer period of 7 days to access the performance stability of our MD device.

The Pt-MBT@Ag NSs/NF spacer was carefully examined using both thermal and SEM-EDX analyses, as shown in Fig. S7a-d. After prolonged MD operation over 7 days, negligible change in either color (Fig. S7a, compare with Fig. 1a) or temperature enhancement caused by the photothermal effect (Fig. S7b, compare with Fig. S4b,ii) was observed. The SEM image (Fig. S7c) and EDX mapping analysis (Fig. S7d) further confirmed that the Pt-MBT@Ag NSs composite remained intact on the 3D porous NF. These observations are expected because of the chemical resistivity of the noble-metal-based material and the strong interaction of the as-synthesized NSs that were directly grown on the NF.

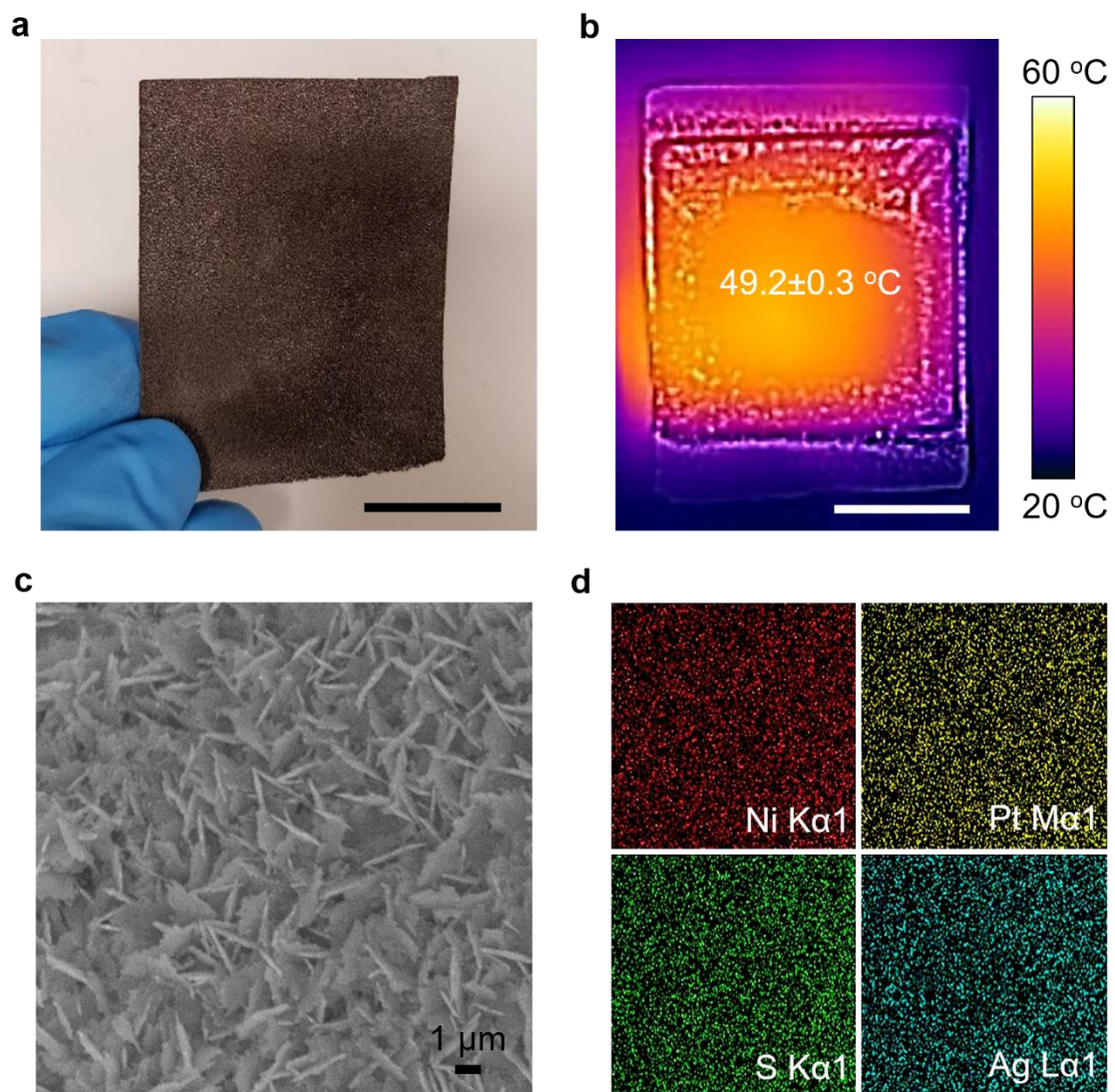


**Fig. S7** a) Photograph of the spacer and its (b) thermal image under light illumination at 0.8 sun in ambient air. Scale bar represents 2 cm for (a-b). c) SEM image of the spacer and its corresponding (d) EDX mapping images, showing the retention of the Pt-MBT@Ag nanostructure.

### S6. Fabrication of lower-cost plasmonic spacer

To lower the material cost of the noble-metal-based spacer, we constructed a more affordable plasmonic absorber by immersing the porous NF in a homogeneously mixed slurry containing the as-obtained Pt-MBT@Ag NSs, cheap carbon black (CB) and polyvinyl alcohol (PVA) binder at a mass of 10 mg, 10 mg and 100 mg, respectively. Before soaking the NF in the plasmonic/binder slurry, the porous NF was first immersed in 3 M HCl solution and sonicated for 30 min, then washed with deionized water several times. To improve the adhesion strength of the plasmonic material on NF, glutaraldehyde (GA) with the same molar ratio as PVA was added as a cross-linker and the polymerization process was catalyzed by mildly acidic condition (0.1 M HCl). Next, the slurry was heated up to 90 °C to evaporate the water, followed by curing at 120 °C for 30 min in the oven. The resulting Pt-MBT@Ag-CB-PVA coated on NF is presented in Fig. S8a. Interestingly, the as-obtained Pt-MBT@Ag-CB-PVA/NF showed similar photothermal effects as compared to the binder-free Pt-MBT@Ag NSs/NF spacer (compare Fig. S8b and Fig. S4bii, respectively), indicating that the former may serve as an alternative candidate for more affordable, energy-efficient solar-enhanced MD.

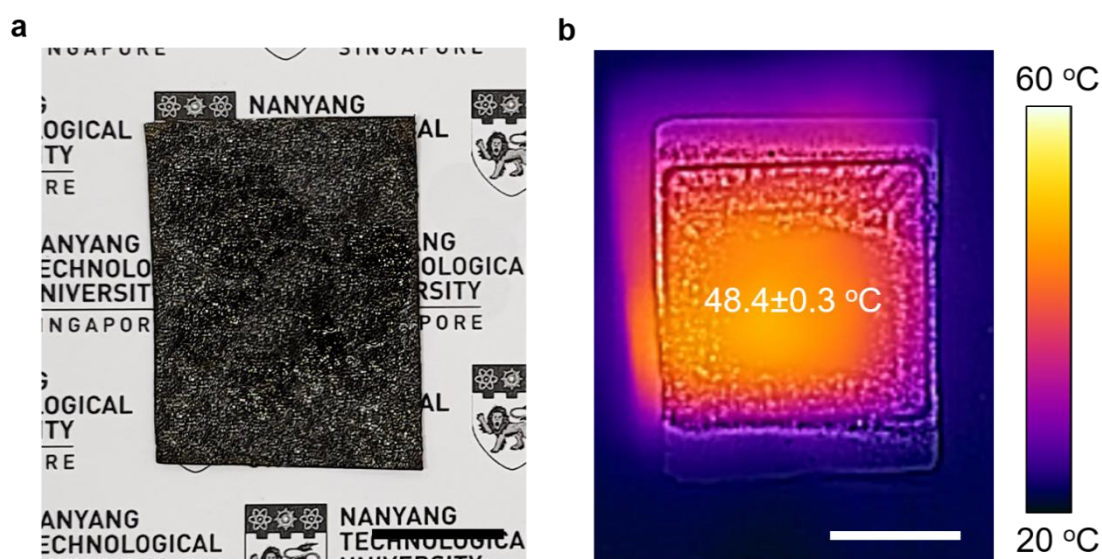


**Fig. S8** a) Photograph of the Pt-CB-PVA NPs/NF spacer and its (b) thermal image under light illumination at 0.8 sun in ambient air. Scale bar represents 2 cm for (a-b).

### S7. Photothermal efficiency of plasmonic spacers

According to the definition of photothermal efficiency,<sup>4</sup>

$$\eta(\%) = \frac{(J_C^1 - J_C^2) \Delta H_{vap}}{I} \times 100 \quad (1)$$

where  $J_C^1$  and  $J_C^2$  are the distillate fluxes with light and without light illumination, respectively,  $\Delta H_{vap}$  is the latent heat of water vaporization, and  $I$  is the solar irradiance intensity. For comparison, the CB-PVA NPs/NF spacer was also fabricated using the method described in Section 6, Supplementary Information. The results (Fig. S9) show that after adding Pt-MBT@Ag NSs into the CB-PVA composite, the photothermal efficiency increased up to 86%, which is slightly lower than that of the binder-free Pt-MBT@Ag NSs/NF spacer ( $\eta = 98\%$ ).

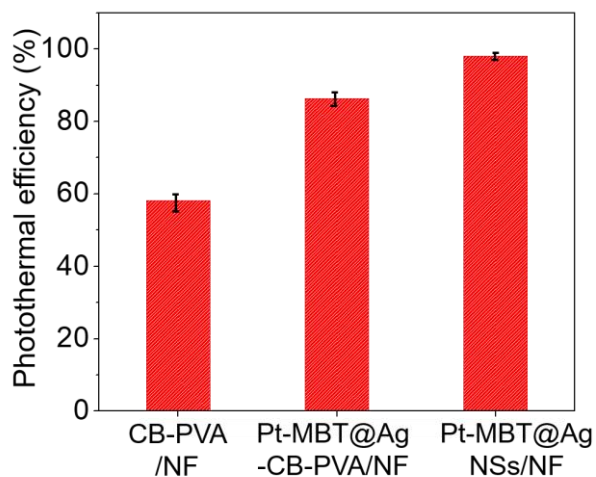


**Fig. S9** Photothermal efficiency of various plasmonic spacers: CB-PVA/NF, Pt-MBT@Ag-CB-PVA/NF, and Pt-MBT@Ag NSs/NF under light illumination at 0.8 sun.

### S8. Stability of binder versus binder-free plasmonic spacers on MD performance

To evaluate the stability of binder versus binder-free plasmonic spacers, the Pt-MBT@Ag-CB-PVA/NF was compared with the Pt-MBT@Ag NSs/NF spacers, respectively. The distillate flux and photothermal efficiency of both spacers were examined in the solar-enhanced MD process under 0.8 sun illumination at a constant feed flowrate of  $250 \text{ ml min}^{-1}$  over 8 h. After 6 h of operation, the Pt-MBT@Ag-CB-PVA/NF spacer (i.e., with binder) exhibited a drastic reduction in distillate flux to  $2.2 \text{ l m}^{-2} \text{ h}^{-1}$  (i.e., lower than the distillate flux of  $2.3 \text{ l m}^{-2} \text{ h}^{-1}$  in the absence of illumination) and photothermal efficiency to 0% (Fig. S10a). This is because the plasmonic material was washed away by the cross-flow shear forces, as indicated in Fig. S10a (inset photograph). In contrast, the Pt-MBT@Ag NSs/NF spacer (i.e., binder-free) not only gave a higher distillate flux ( $3.6 \text{ l m}^{-2} \text{ h}^{-1}$ ) and photothermal efficiency ( $\sim 98\%$ ), but also was able to maintain the high performance throughout the 8 h. The stability of binder-free Pt-MBT@Ag NSs/NF spacer is attributed to the strong Pt-Ni interaction at the absorber-NF interface, as proven in Fig. S10b (inset), showing that the plasmonic material still remained intact on the NF at the end of the 8 h.

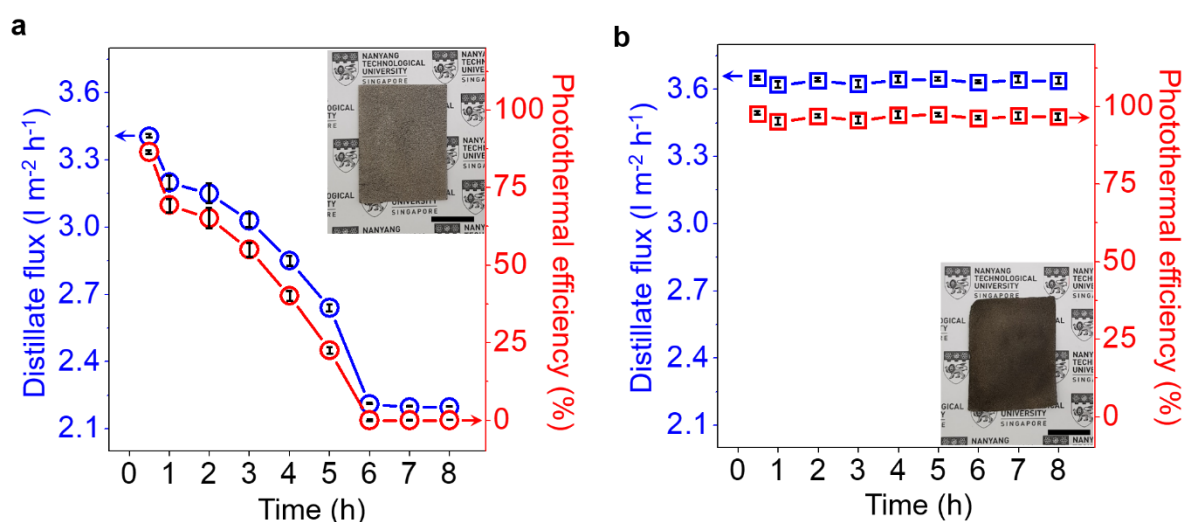


**Fig. S10** Distillate flux and photothermal efficiency of a) Pt-MBT@Ag-CB-PVA (i.e., with binder)/NF versus b) binder-free Pt-MBT@Ag NSs/NF spacers over 8 h of solar-enhanced MD under light illumination at 0.8 sun and at a  $250 \text{ ml min}^{-1}$  feed flowrate. The photograph of each spacer after 8 h is shown in the inset of the respective plot. All the tests were done with saline solution (0.5 M NaCl). Scale bar represents 2 cm for (a-b).

Notably, at the end of 8 h, black solid particles were found on the PVDF membrane when the Pt-MBT@Ag-CB-PVA/NF spacer (i.e., with binder) was used (Fig. S11a). Further examination of the black solid particles with SEM in combination with EDX line scan confirmed that the particles were Pt-MBT@Ag-CB-PVA composites (Fig. S11b-c), which were sheared off by the cross-flowing feed and thereby resulted in the deterioration of the MD performance (Fig. S10a). In addition, the distillate flux decreased to that below the absence of illumination because the loose black solid particles blocked the pores. In contrast, for the binder-free Pt-MBT@Ag NSs/NF spacer, no loose particles were observed (Fig. S11d-f), further proving the excellent stability of our plasmonic spacer.

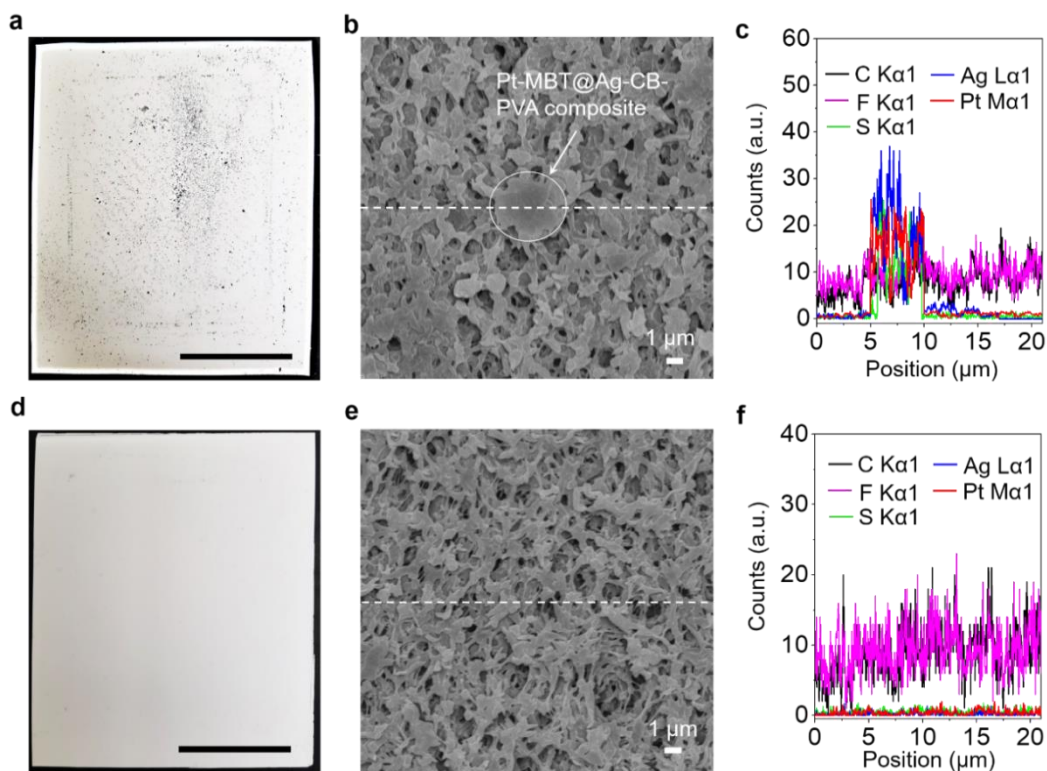


**Fig. S11** Evaluation of the plasmonic spacers on the PVDF membrane after 8 h of continuous MD operation under 0.8 sun illumination at a feed flowrate of  $250 \text{ ml min}^{-1}$ . a) Photograph of PVDF membrane used with the Pt-MBT@Ag-CB-PVA/NF spacer (i.e., with binder) and its corresponding (b) SEM image: dash line represents the EDX line scan position in (c), while the solid circle shows that the Pt-MBT@Ag-CB-PVA composite was found on the PVDF membrane surface, as deduced from the EDX line scan in (b). d) Photograph of PVDF membrane used with the binder-free Pt-MBT@Ag NSs/NF spacer and its corresponding (e) SEM image: dash line represents the EDX line scan position in (f). Scale bar represents 2 cm for (a and d).

### S9. Solar-enhanced MD performance at various Reynolds number

Fig. S12 illustrates the relationship between distillate flux and Reynolds number for the various plasmonic spacers. The Reynolds number ( $Re$ ) is calculated using the following equation:

$$Re = ud_h\gamma$$

where  $u$  is the velocity of the feed flowrate,  $d_h$  is the hydraulic diameter of a rectangular duct with dimensions (0.4 cm  $\times$  5.3 cm) and  $\gamma$  is the kinematic viscosity ( $7.2 \times 10^{-7} \text{ m}^2 \text{ s}^{-1}$ ) of water at 35 °C. The distillate flux was  $\sim 8 \text{ l m}^{-2} \text{ h}^{-1}$  at high Reynolds number of  $\sim 1600$  investigated under 0.8 sun illumination. The results affirm the positive relationship between Reynolds number and distillate flux, which implies that the performance of the solar-enhanced MD can be further enhanced when the Reynolds number increases. Notably, such high Reynolds number would not be possible for the binder-based plasmonic spacers (Section S8, Supplementary Information), which thereby highlights the unique advantage of our binder-free plasmonic spacers under high shear conditions (see Movie S2, Supplementary Information, whereby the feed flowrate was 2000 ml min<sup>-1</sup>).

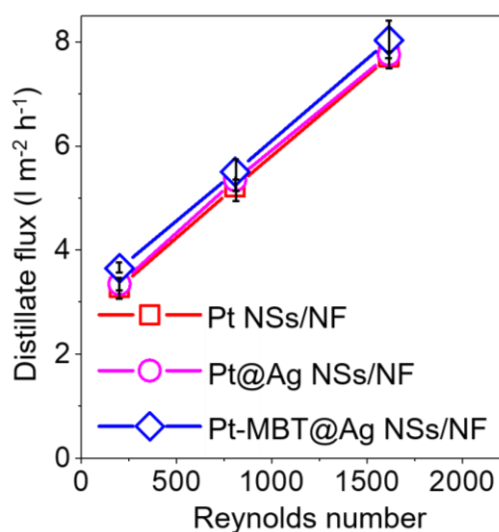


**Fig. S12** Distillate flux as function of various Reynolds number for different plasmonic spacers. The inlet feed temperature was 35 °C and the illumination was 0.8 sun.

### S10. Photothermal efficiencies comparison

To further demonstrate the excellent solar-enhanced MD performance conferred by our plasmonic spacers, we compared them with other advanced solar absorbers, which include polymer, carbon, graphene, ceramic, and noble-metal-based materials. So far, most of the photothermal efficiencies were reported for vapor evaporator applications<sup>5-14</sup> and a handful of reports revealed the photothermal efficiencies in solar MD process.<sup>[4,15]</sup> As is well-acknowledged, the natural sunlight on the Earth's surface is estimated to be  $\sim 1$  sun, so typically, expensive optical concentrators are required to enable solar desalination. Despite the costly optical concentrator inflating the total capital cost,<sup>16</sup> it remains a challenge to create an efficient absorber without the use of optical concentrators. Fig. S13 shows that most absorbers have photothermal efficiencies below 70% under  $\sim 1$  sun irradiance (in the blue region of Fig. S13), except Ref. [4,11], while the rest of the absorbers reported with efficiencies above 70% required the use of optical concentrators (in the red region of Fig. S13). Benchmarked against past studies, our plasmonic absorbers exhibited excellent photothermal efficiencies of more than 70% even at illumination of below 1 sun irradiance. Among them, the Pt-MBT@Ag NSs/NF spacer had the highest photothermal efficiency of 98%, which is the highest ever reported so far. This excellent performance can be attributed to the presence of the nano-ligand (MBT), which created nano-gaps at the Pt-Ag interface that generated thermal hot spots (localization of excess temperature),<sup>3</sup> leading to a significant enhancement of photothermal effects in the Pt-MBT@Ag spacer. In addition, the unique 3D structure also helped to disseminate heat easily throughout the whole spacer, maximizing the localized heating effect for improved photothermal efficiency.

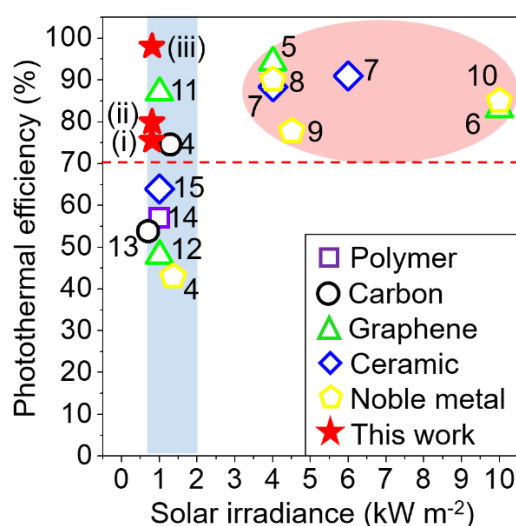


**Fig. S13** Comparison of photothermal efficiencies. The photothermal efficiency against solar irradiance data were extracted from literature, along with experimental data obtained in this work. (i), (ii), and (iii) represent Pt NSs/NF, Pt@Ag NSs/NF, and Pt-MBT@Ag NSs/NF in this work, respectively. Data points from Ref. [5-10] in the red colored region are absorbers functional under more than 1 sun (i.e., optical concentrator required), while the red dash line is the photothermal efficiency cut-off at 70%. Data points from Ref. [4, 11-15] in the blue colored region are absorbers functional under  $\sim 1$  sun (i.e., direct sunlight at Earth's surface).

### S11. Energy consumption of 3D porous spacers

The energy consumption of solar-enhanced MD was calculated using the following equation:

$$\text{Energy consumption} = \frac{E}{V} \quad (2)$$

where  $E$  is the energy used by the heater during the MD process and  $V$  is the distillate volume. We have measured the energy consumed using a power meter installed on the heater (see Fig. S3b). In the absence of illumination, all the spacers exhibited similar energy consumption at  $\sim 5.0 \text{ kWh l}^{-1}$ . Upon light illumination at 0.8 sun, the pristine NF had a negligible effect on energy consumption. On the other hand, the energy consumption of the plasmonic Pt NSs/NF and Pt@Ag NSs/NF spacers decreased by approximately 34%, while the Pt-MBT@Ag NSs/NF spacer further reduced the energy consumption to as low as  $2.5 \text{ kWh l}^{-1}$ , which is almost half that in the absence of illumination. The enhanced energy efficiency was enabled by the localized excess heating derived from thermal hot spots.

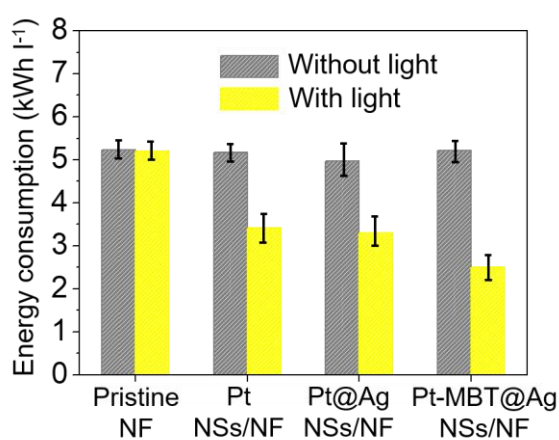


**Fig. S14** Energy consumption during MD. MD was carried out in the absence and presence of illumination at 0.8 sun. The feed was 0.5 M NaCl and the feed flowrate was  $250 \text{ ml min}^{-1}$ .

## References

- S1 C. F. Bohren, D. R. Huffman, *Absorption and Scattering of Light by Small Particles*. (WILEY-VCH Verlag GmbH & Co. KGaA, 2007).
- S2 A. S. Hassanien and A. A. Akl, *J. Alloys Compd.*, 2015, **648**, 280-290.
- S3 M. S. Zielinski, J-W Choi, T. L. Grange, M. Modestino, S. M. H. Hashemi, Y. Pu, S. Birkhold, J. A. Hubbell and D. Psaltis, *Nano Lett.*, 2016, **16**, 2159-2167.
- S4 J. Wu, K. R. Zodrow, P. B. Szemraj and Q. Li, *J. Mater. Chem. A.*, 2017, **5**, 23712-23719.
- S5 P. Zhang, J. Li, L. Lv, Y. Zhao and L. Qu, *ACS Nano*, 2017, **11**, 5087-5093.
- S6 J. Qisheng, L. Tian, S. Tadepalli, R. Raliya, P. Biswas, R. R. Naik and S. Singamaneni, *Adv. Mater.*, 2016, **28**, 9400-9407.
- S7 L. Zhou, Y. Tan, J. Wang, W. Xu, Y. Yuan, W. Cai, S. Zhu and J. Zhu, *Nature Photonics.*, 2016, **10**, 393-398.
- S8 L. Zhou, Y. Tan, D. Ji, B. Zhu, P. Zhang, J. Xu, Q. Gan, Z. Yu and J. Zhu, *Sci. Adv.*, 2016, **2**, e1501227.
- S9 L. Yanming, S. Yu, R. Feng, A. Bernard, Y. Liu, Y. Zhang, H. Duan, W. Shang, P. Tao, C. Song and T. Deng, *Adv. Mater.*, 2015, **27**, 2768-2774.
- S10 Z. Mingwei, Y. Li, F. Chen, X. Zhu, J. Dai, Y. Li, Z. Yang, X. Yan, J. Song, Y. Wang, E. Hitz, W. Luo, M. Lu, B. Yang and L. Hu, *Adv. Energy Mater.*, 2018, **8**, 1701028.
- S11 Y. Yang, R. Zhao, T. Zhang, K. Zhao, P. Xiao, Y. Ma, P. M. Ajayan, G. Shi and Y. Chen, *ACS Nano*, 2018, **12**, 829-835.
- S12 J. Yang, Y. Pang, W. Huang, S. K. Shaw, J. E. Schiffbauer, M. A. Pillers, X. Y. Mu, S. Luo, T. Zhang, Y. Huang, G. Li, S. Ptasinska, M. Lieberman and T. Luo, *ACS Nano*, 2017, **11**, 5510-5518.
- S13 G. Ni, S. H. Zandayi, S. M. Javid, S. V. Boriskina, T. A. Cooper and G. Chen, *Energy Environ. Sci.*, 2018, **11**, 1510-1519.
- S14 G. Ni, G. Li, S. V. Boriskina, H. Li, W. Yang, T. J. Zhang and G. Chen, *Nat. Energy*, 2016, **1**, 16126.
- S15 P. D. Dongare, A. Alabastri, S. Pedersen, K. R. Zodrow, N. J. Hogan, O. Neumann, J. Wu, T. Wang, A. Deshmukh, M. Elimelech, Q. Li, P. Nordlander and N. J. Halas, *Proc. Natl Acad. Sci. USA*, 2017, **114**, 6936-6941.
- S16 L. A. Weinstein, J. Loomis, B. Bhatia, D. M. Bierman, E. N. Wang and G. Chen, *Chem. Rev.*, 2015, **115**, 12797-12838.